# Electronic supplenmentary information for

## Improved Photoelectrochemical Performances over Electrochemically Reduced $WO_3$: Implications of Oxygen Vacancies

Yunni Liu, Wang Yao, Jun Lin*

Department of Chemistry, Renmin University of China, Beijing 100872, P. R. China.

Email: jlin@ruc.edu.cn

### 1. Calculation of charge separation and charge injection efficiency [1, 2]

The photocurrent density generated by PEC water oxidation can be described by the following formula:

$$J_{PEC} = J_{absorbed} \times P_{charge\ separation} \times P_{charge\ injection}$$

Where $J_{absorbed}$ is the photocurrent density generated by the complete conversion of the the absorbed irradiation absorbed by the material, which is constant with fixed semiconductor photocatalyst and lighting source. $P_{charge\ separation}$ is the charge separation yield of the photogenerated charge carriers. $P_{charge\ injection}$ is the charge injection yield from electrode to electrolyte, which reflects the efficiency of water oxidation process. This equation reflects the energy loss in different reaction processes of PEC water oxidation reaction.

To obtain detailed information on the efficiency of each process, the widely used hole scavenger $Na_2SO_3$ (0.1 M) was added to the electrolyte (0.5 M $Na_2SO_4$), and all the holes collected on the surface were consumed. By this way, the charge injection efficiency was 100% to further determine the charge separation efficiency. As described above:

$$J_{Na_2SO_3} = J_{absorbed} \times P_{charge\ separation}$$

Therefore, the charge separation and charge injection efficiency can be calculated as follows:

$$P_{\text{charge separation}} = J_{Na_2SO_3} / J_{\text{absorbed}}$$

$$P_{\text{charge injection}} = J_{\text{water}} / J_{Na_2SO_3}$$

**2. Calculation of the carrier concentrations ($N_D$ )and the width of space charge layer ($d_{SC}$) [1, 3, 4]**

The carrier concentrations can be calculated quantitatively according to the Mott-Schottky equation as below：

$$\frac{1}{C^2} = \frac{2}{N_D e\varepsilon\varepsilon_0}(E - E_{fb} - \frac{KT}{e})$$

The constant C on the left side of the formula is the space charge capacitance in the semiconductor, while the constants $N_D$, e, $\varepsilon_0$ and ε on the right side of the formula are the carrier density, elemental charge, permittivity of a vacuum and relative permittivity of the semiconductor, respectively. The constants E, $E_{fb}$, T and k in parentheses are the applied potential, flat band potential, temperature and Boltzmann constant, respectively. In addition, the carrier density ($N_D$) and the width of space charge layer ($d_{SC}$) could also be quantified by the following equation:

$$N_D = \frac{2}{e\varepsilon_0\varepsilon}\left(\frac{dE}{d\left(\frac{1}{C^2}\right)}\right)$$

$$d_{sc} = \sqrt{\frac{2\varepsilon\varepsilon_0\left(E - E_{fb}\right)}{eN_D}}$$

where e = 1.6 × $10^{-19}$ C, K = 1.38× $10^{-23}$ J/K, T = 298 K, $\varepsilon_0$ = 8.86 × $10^{-12}$ F/m and ε = 20 F/m for $WO_3$.

**3. The measurement of electrochemical surface area (ECSA) [5, 6]**

The ECSA values were estimated by determining the double-layer capacitance of the system from CV. First, a non-Faradaic region was identified from CV in quiescent solution. And all the measured currents in this region were assumed to be from the double-layer charging. Based on this assumption, the charging current ($i_c$) was equal to the product of electrochemical double layer capacitance, $C_{dl}$ and the scan rate (v), as shown in the following equation:

$$i_c = v\,C_{dl}$$

Plotting $i_c$ as a function of v yields a straight line with a slope of $C_{dl}$. So, the ESCA of the photoelectrode can be calculated through dividing $C_{dl}$ by the specific capacitance of the sample as shown in in the following equation:

$$ECSA = \frac{C_{dl}}{C_s}$$

Here we used a general specific capacitance of 0.040 mF $cm^{-2}$ for the metal oxide.

**4. The specific optimization processes of photoanode materials**

The electrochemical reduction voltage and time of $WO_3$ were optimized with respect to the PEC performances for RhB degradation and $H_2$ evolution. As shown in **Fig. S1-2**, the $WO_3$ photoanode exhibited the highest PEC performances for the RhB degradation and $H_2$ evolution after the electrochemical reduction at 3.76 V *vs.* NHE for 60 min. The optimized conditions were also supported by FESEM observations (**Fig. S3**). When the electrochemical reduction voltage exceeds 3.76 V *vs.* NHE, or the electrochemical reduction time was extended for more than 60 min, as observed in **Fig. S4-5**, the monoclinic structure of $WO_3$ was maintained, but it porous cotton-like morphology collapses, which might be detrimental to a PEC process.

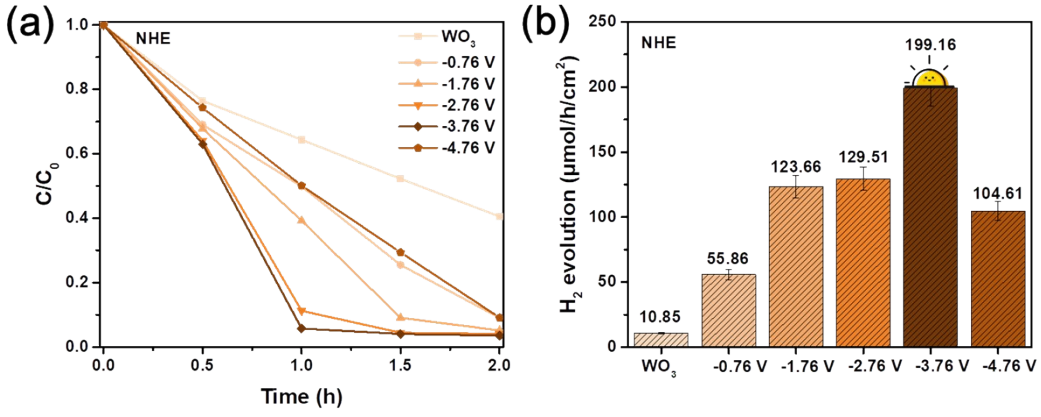


**Fig. S1.** (a) PEC RhB degradation and (b) $H_2$ evolution rate over the $WO_3$ photoanodes electrochemically reduced under different voltages for 40 min.

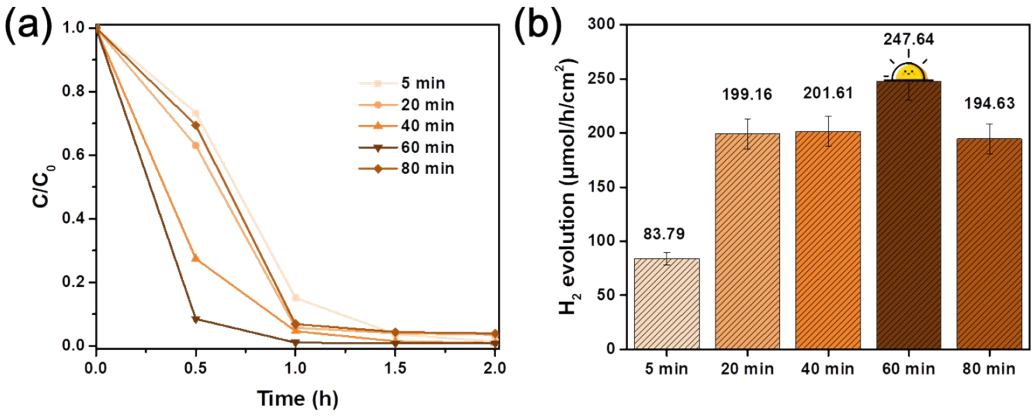


**Fig. S2.** (a) PEC RhB degradation and $H_2$ evolution rate over the $WO_3$ photoanodes electrochemically reduced under -3.76 V *vs.* NHE for different time.

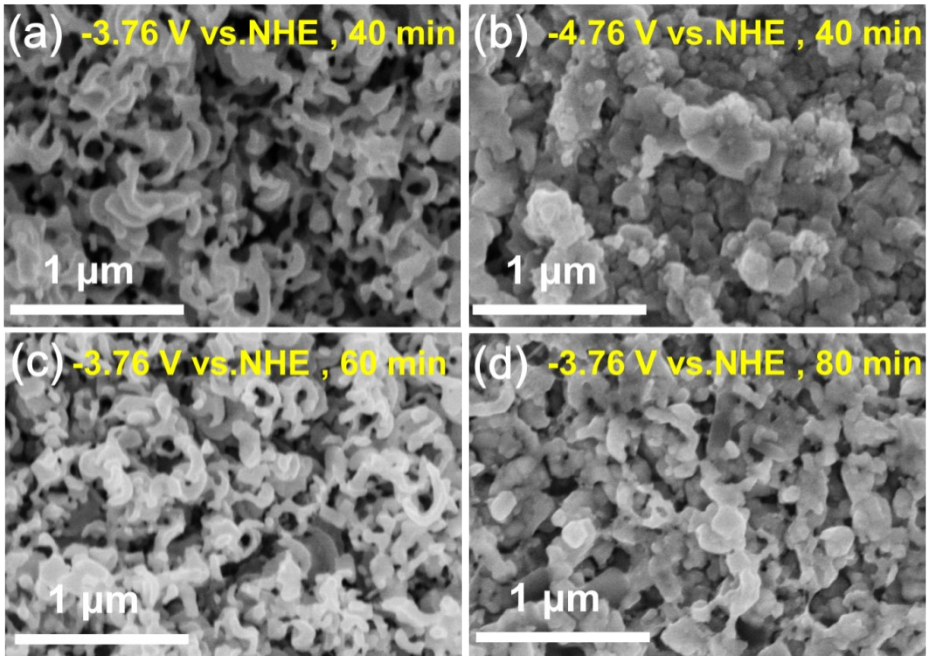


**Fig. S3.** FESEM images of the porous cotton-like $WO_3$ photoanodes electrochemically reduced under different conditions: (a) -3.76 V *vs.* NHE for 40 min, (b) -4.76 V *vs.* NHE for 40 min, (c) -3.76 V *vs.* NHE for 60 min, (d) -3.76 V *vs.* NHE for 80 min.

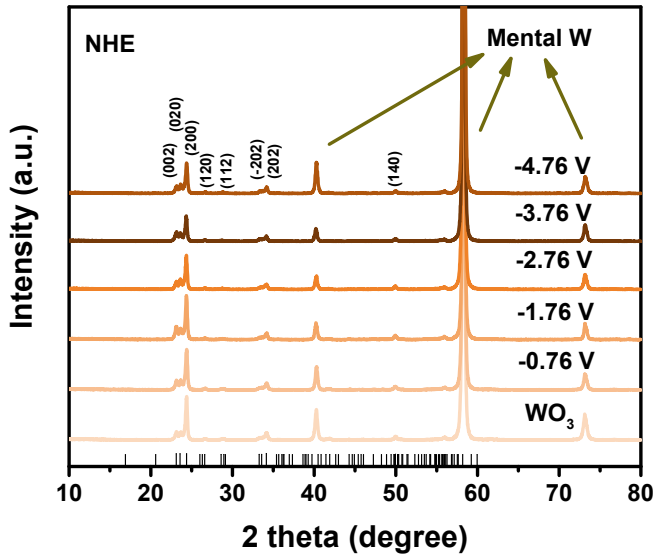


**Fig. S4.** XRD patterns of the samples with different electrochemical reduction voltages..

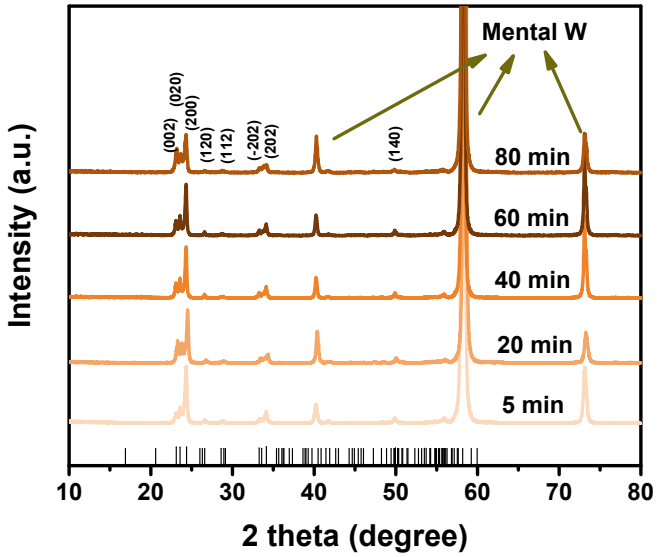


**Fig. S5.** XRD patterns of the samples with different electrochemical reduction times.

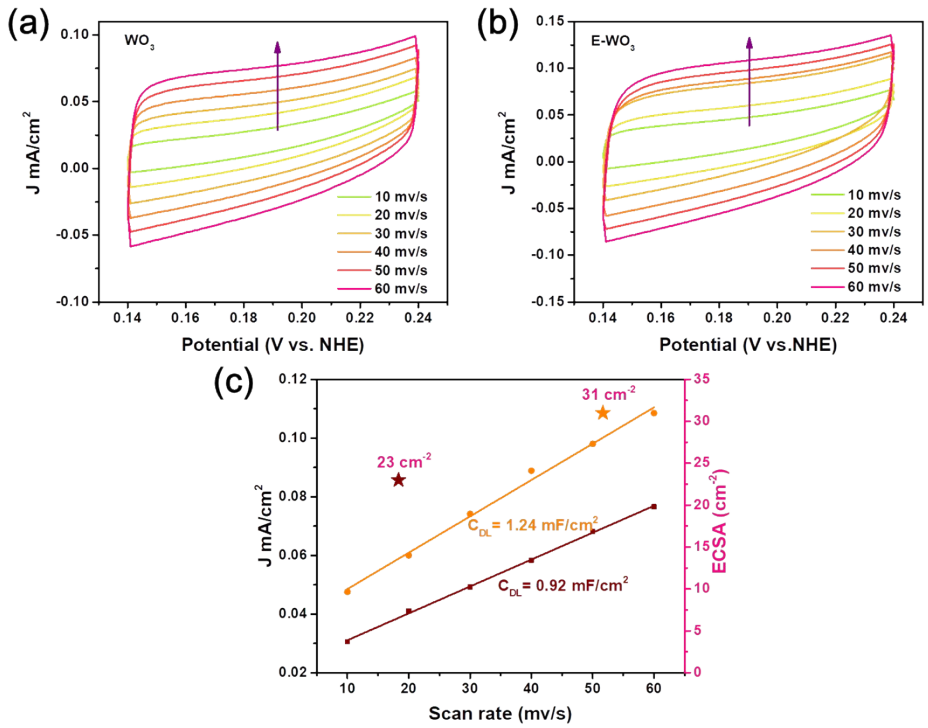


**Fig. S6.** Cyclic voltammograms of (a) $WO_3$ and (b) E-$WO_3$ photoanodes respectively. (c) Electrochemical surface area measurements of $WO_3$ and E-$WO_3$ photoanodes.

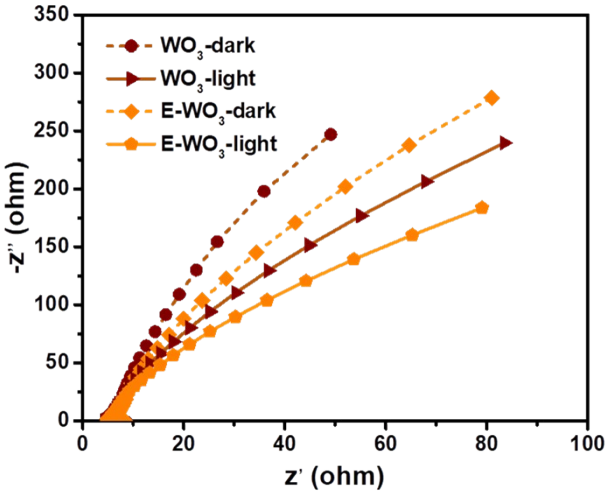


**Fig. S7.** Nyquist plots of the $WO_3$ and E-$WO_3$ photoanodes at open circuit voltage.

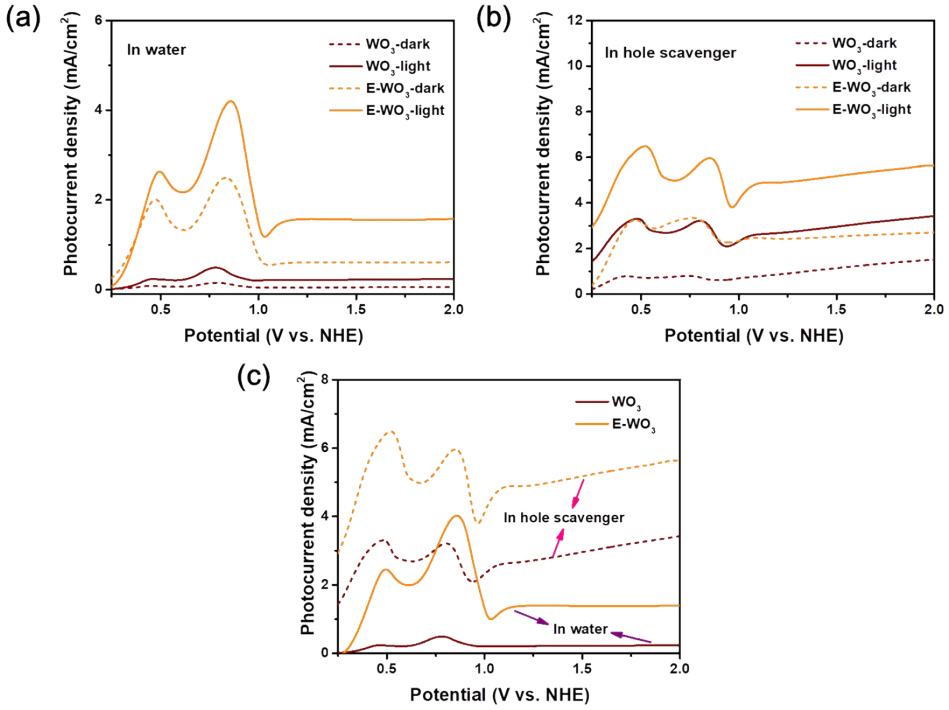


**Fig. S8.** The linear sweep voltammetry (LSV) measured by $WO_3$ and E-$WO_3$ photoanodes (a) in 0.5 M $Na_2SO_4$ solution (in water) and (b-c) with a further addition of 0.1 M $Na_2SO_3$ solution (in hole scavenger).

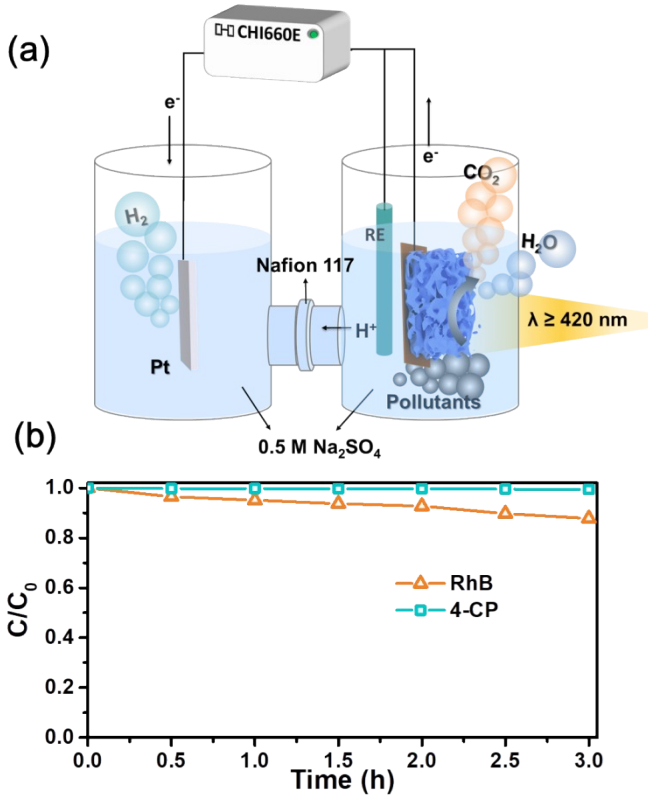


**Fig. S9.** (a) Schematic illustration for PEC system using the E-$WO_3$ photoanode. (b) Degradation efficiencies of different pollutants (RhB, and 4-CP) under light irradiation without any catalysts.

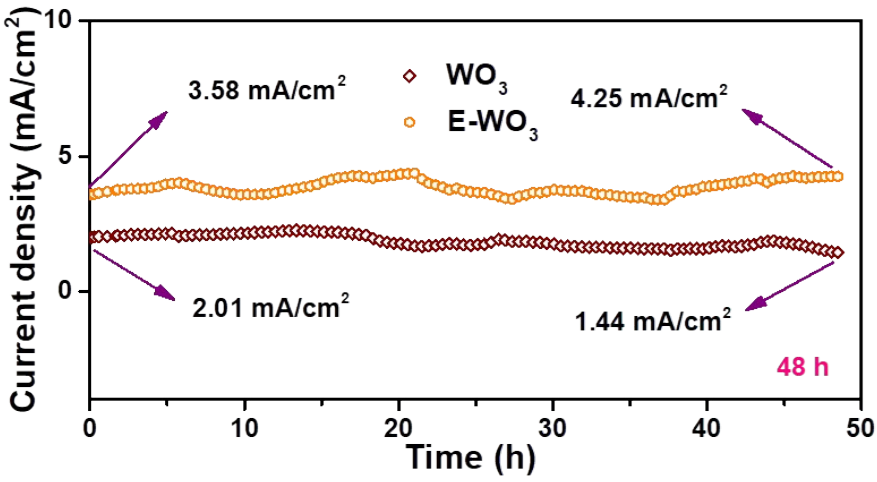


**Fig. S10.** The current density stability tests for $WO_3$ and E-$WO_3$ photoanodes in an aqueous solution of $Na_2SO_4$ (0.5 M).

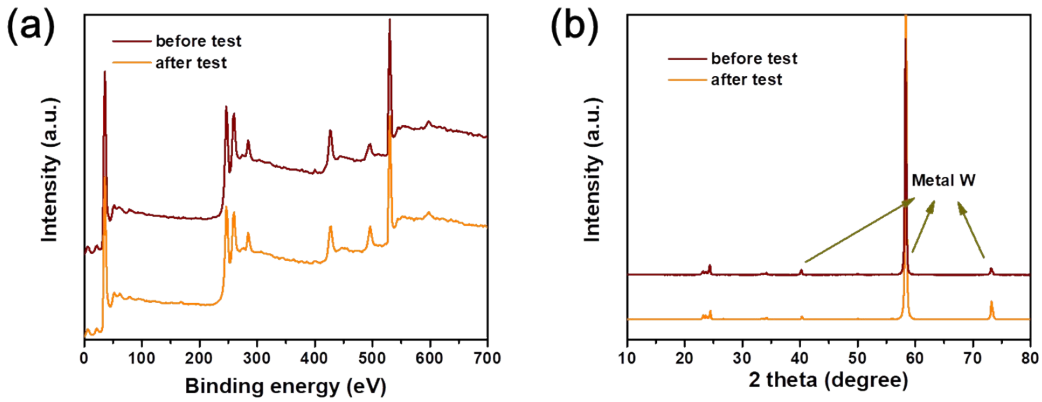


**Fig. S11.** (a) XRD patterns (b) XPS survey spectra of the E-$WO_3$ photoanode after ten cycles of 2 h activity tests.

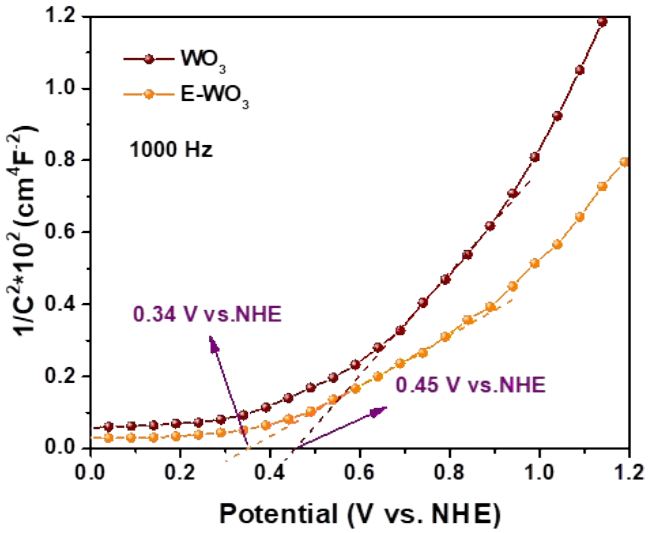


**Fig. S12.** Mott-Schottky plots of $WO_3$ and E-$WO_3$ photoanodes measured at fixed frequencies of 1000 Hz.

**Table S1.** Fitting results of Mott-Schottky plots and indirect inter-band transition energy for the $WO_3$ and E-$WO_3$ photoanodes.

| **Samples** | $E_{fb}$ | $E_{CB}$ | ***Eg*** **(eV)** | $E_{VB}$ |
|---|---|---|---|---|
| $WO_3$ | 0.45 | 0.02 | 2.70 | 2.72 |
| E-$WO_3$ | 0.34 | -0.04 | 2.70 | 2.66 |

**Table S2.** The carrier concentrations ($N_D$) in $WO_3$ and E-$WO_3$ photoanodes obtained by Mott-Schottky plots measured at 1000 Hz and space charge layer ($d_{SC}$) values.

| **Samples** | **$WO_3$** | **E-$WO_3$** |
|---|---|---|
| $N_D$ ($cm^{-3}$) | $7.49\times10^{28}$ | $1.25\times10^{29}$ |
| $d_{SC}$ (nm) | 9.42 | 8.21 |

**Table S3.** The overview on the application of different $WO_3$ based photoanodes with different morphologies in PEC field.

| **Morphology/crystal structure** | **Synthesis method** | **Electrolyte** | **Photocurrent** | **$H_2$ and $O_2$ evolution/ Pollutants removal** | **References** |
|---|---|---|---|---|---|
| Nanorod, columnar, tree like columnar/ monoclinic | Pulsed laser deposition | 0.1 M $Na_2SO_4$ | 1.9 mA/$cm^2$ at 1.6 V *vs.* RHE | $H_2$: 14.8 µmol*$h^{-1}$ $O_2$: - | [7] |
| Layered porous microstructur/ monoclinic | RF plasma sputtering | 0.5 M $Na_2SO_4$ + 1.2 M $CH_3OH$ | 6.3 mA/$cm^2$ at 1.0 V *vs.* SCE | $H_2$: 187.6 µmol*$h^{-1}$ $O_2$: 93.2 µmol*$h^{-1}$ | [8] |
| 3D nanowalls/ monoclinic | Hydrothermal | 0.1 M $Na_2SO_4$ | 1.61 mA/$cm^2$ at 1.23 V *vs.* RHE | $H_2$: - $O_2$: - | [9] |
| Nanorods/ monoclinic | Two-step flame heating | 0.1 M $Na_2SO_4$ | 1.06 mA/$cm^2$ at 1.23 V *vs.* RHE | $H_2$: - $O_2$: - | [10] |
| Nanoplate/ monoclinic | Chemical bath deposition method | 10 mg/L 4-CP + 0.1 M $Na_2SO_4$ | 1.38 mA/$cm^2$ at 1.2 V vs SHE | 98.9 % 4-CP | [11] |
| Nanoplate/ monoclinic | Modified hydrothermal | 10 mg/L Phenol + 0.1 | 2.37 mA/$cm^2$ at 1 V *vs.* SCE. | 58 % Phenol | [12] |

| | | | | | |
|---|---|---|---|---|---|
| | method | M KPB | | | |
| Dense layer, nanoplate arrays, tiny particles/ monoclinic | Hydrothermal | 0.5 M $Na_2SO_4$ | 1.81 mA/cm$^2$ at 1.23 V *vs.* RHE | $H_2$: - $O_2$: - | [13] |
| Porous coral-like/ monoclinic | Anodic oxidation | 5 mg/L RhB, MB, 4-CP, BPA and PFOA + 0.5 M $Na_2SO_4$ | 0.31 mA/cm$^2$ at 0.5 V *vs.* Ag/AgCl | $H_2$: 16.05 μmol*h$^{-1}$ 100 % RhB, 90 % MB, 60 % MO, 19.2 % 4-CP, 57.1 % BPA and 44.2 % PFOA | [14] |
| Nanoplates and hexagonal prisms/hexagonal-monoclinic phase junction | a two-step hydrothermal method | 20 mg/L BPA +0.1 M $Na_2SO_4$ | 5.6 mA/cm$^2$ at 1.2 V *vs.* RHE | 99.8 % of BPA | [15] |
| Nanoplate/ single crystal | Chemical bath deposition method | 20 mg/L TC-HCl + 1 M $Na_2SO_4$ | 1.4 mA/cm$^2$ at 1.23 V *vs.* RHE | 99 % TC-HCl, 97.8 % NOR | [16] |
| Porous cotton-like/ monoclinic | Anodic oxidation | 10 mg/L RhB, MO, MB, 4-CP + 0.5 M $Na_2SO_4$ | 3.9 mA/cm$^2$ at 0.5 V *vs.* SCE | $H_2$: 226.81 μmol*h$^{-1}$*cm$^{-2}$ 100 % dyes and 90.8 % 4-CP | Our work |

**References**


[1] S. Kim, S. Ji, K.H. Kim, S.H. Roh, Y. Cho, C.-L. Lee, K.-S. Lee, D.-G. Choi, H. Choi, J.K. Kim, J.H. Park, Revisiting surface chemistry in $TiO_2$: A critical role of ionic passivation for pH-independent and anti-corrosive photoelectrochemical water oxidation, Chem. Eng. J., 407 (2021) 126929.

[2] R. Zhang, F. Ning, S. Xu, L. Zhou, M. Shao, M. Wei, Oxygen vacancy engineering of $WO_3$ toward largely enhanced photoelectrochemical water splitting, Electrochim. Acta, 274 (2018) 217-223.

[3] Y. Liu, Q. Li, Z. Lian, J. Fan, Y. Tao, G. Li, H. Li, Polarization field promoted photoelectrocatalysis for synergistic environmental remediation and $H_2$ production,

Chem. Eng. J., 437 (2022) 135132.

[4] M. Tayebi, B.-K. Lee, The effects of W/Mo-co-doped $BiVO_4$ photoanodes for improving photoelectrochemical water splitting performance, Catal. Today, 361 (2021) 183-190.

[5] J.D. Benck, Z. Chen, L.Y. Kuritzky, A.J. Forman, T.F. Jaramillo, Amorphous Molybdenum Sulfide Catalysts for Electrochemical Hydrogen Production: Insights into the Origin of their Catalytic Activity, ACS Catal., 2 (2012) 1916-1923.

[6] C.C.L. McCrory, S. Jung, I.M. Ferrer, S.M. Chatman, J.C. Peters, T.F. Jaramillo, Benchmarking Hydrogen Evolving Reaction and Oxygen Evolving Reaction Electrocatalysts for Solar Water Splitting Devices, J. Am. Chem. Soc., 137 (2015) 4347-4357.

[7] M. Mai, X. Ma, H. Zhou, M. Ye, T. Li, S. Ke, P. Lin, X. Zeng, Effect of oxygen pressure on pulsed laser deposited $WO_3$ thin films for photoelectrochemical water splitting, J. Alloys Compd., 722 (2017) 913-919.

[8] G.L. Chiarello, M. Bernareggi, M. Pedroni, M. Magni, S.M. Pietralunga, A. Tagliaferri, E. Vassallo, E. Selli, Enhanced photopromoted electron transfer over a bilayer $WO_3$ n–n heterojunction prepared by RF diode sputtering, J. Mater. Chem. A, 5 (2017) 12977-12989.

[9] W. Tian, C. Chen, L. Meng, W. Xu, F. Cao, L. Li, PVP Treatment Induced Gradient Oxygen Doping in $In_2S_3$ Nanosheet to Boost Solar Water Oxidation of $WO_3$ Nanoarray Photoanode, Adv. Energy Mater., 10 (2020) 1903951.

[10] C. Shao, A.S. Malik, J. Han, D. Li, M. Dupuis, X. Zong, C. Li, Oxygen vacancy engineering with flame heating approach towards enhanced photoelectrochemical water oxidation on $WO_3$ photoanode, Nano Energy, 77 (2020) 105190.

[11] X. Liu, H. Zhou, S. Pei, S. Xie, S. You, Oxygen-deficient $WO_{3-x}$ nanoplate array film photoanode for efficient photoelectrocatalytic water decontamination, Chem. Eng. J., 381 (2020) 122740.

[12] Q. Zeng, Y. Gao, L. Lyu, S. Chang, C. Hu, Highly improved photoelectrocatalytic efficiency and stability of $WO_3$ photoanodes by the facile in situ growth of $TiO_2$ branch overlayers, Nanoscale, 10 (2018) 13393-13401.

[13] Z. Ma, H. Hou, K. Song, Z. Fang, L. Wang, F. Gao, W. Yang, B. Tang, Y. Kuang, Engineering oxygen vacancies by one-step growth of distributed homojunctions to enhance charge separation for efficient photoelectrochemical water splitting, Chem. Eng. J., 379 (2020) 122266.

[14] D. Pan, S. Xiao, X. Chen, R. Li, Y. Cao, D. Zhang, S. Pu, Z. Li, G. Li, H. Li, Efficient Photocatalytic Fuel Cell via Simultaneous Visible-Photoelectrocatalytic Degradation and Electricity Generation on a Porous Coral-like $WO_3$/W Photoelectrode, Environ. Sci. Technol., 53 (2019) 3697-3706.

[15] Q. Ma, R. Song, F. Ren, H. Wang, W. Gao, Z. Li, C. Li, Photoelectrocatalytic degradation of refractory pollutants over $WO_3$/W network photoelectrode with heterophase junction for enhancing mass transportation and charge separation, Appl. Catal. B Environ., 309 (2022) 121292.

[16] J. Wang, L. Jiang, F. Liu, M. Jia, M. Liu, J. Li, Y. Lai, Enhanced photoelectrochemical degradation of tetracycline hydrochloride with FeOOH and Au nanoparticles decorated $WO_3$, Chem. Eng. J., 407 (2021) 127195.